

# Aeroacoustic Investigation of an Open Cavity at Low Mach Number

Johan Larsson\*

Volvo Car Corporation, S-40508 Göteborg, Sweden

Lars Davidson†

Chalmers University of Technology, S-41296 Göteborg, Sweden

Magnus Olsson‡

Volvo Car Corporation, S-40508 Göteborg, Sweden

and

Lars-Erik Eriksson§

Chalmers University of Technology, S-41296 Göteborg, Sweden

The laminar flow and the near-field acoustics of an open cavity at Mach number 0.15 is computed by direct solution (two-dimensional) of the compressible Navier–Stokes equations. The radiated sound is also computed by an acoustic analogy, a modified version of Curle’s equation, and compared to the directly computed sound field. The agreement is found to be good. The contributions from the various source terms in Curle’s equation are quantified, and the terms involving wall-pressure fluctuations are found to account for most of the radiated intensity. These main source terms are investigated further, and it is found that they are especially large in the downstream part of the cavity, and for about two cavity lengths downstream of the cavity. The upstream dominance of the radiated sound is explained by the fact that the downstream cavity wall contributes primarily to the upstream direction. Correlations between the radiated sound and the source terms, coupled with where the source terms are large, suggest that the near-field terms display a stronger upstream dominance than the far-field terms, and hence the far-field directivity is expected to be flatter.

## I. Introduction

**A**EROACOUSTICS, or the sound generated by fluid flows, is an area of research that has received an increasing amount of attention during the past decade. Most of the research has been aimed at high-Mach-number applications, with jet noise being the most typical case of interest. With the increases in performance of computers, the numerical simulation of aeroacoustics, or computational aeroacoustic (CAA), has become more popular.

The interest for aeroacoustics in the vehicle industry has increased during the last few years, primarily because of customer surveys that show wind noise to be a common complaint. In vehicle applications, the Mach numbers of the flows are typically small, and the flows are often heavily separated because of the complex geometries present.

The motion in a compressible fluid is determined by the governing equations, together with proper boundary conditions. While being a trivial remark, this means that the acoustics and the flow are intrinsically coupled, and it is, on a philosophical level, not possible to think of acoustics and flow as two separate phenomena. For many cases, however, it is possible to split the problem in two parts: the fluid flow problem and the acoustic problem. If the problem can be

split, there are two main approaches to describe the acoustic part of the problem: by a scalar equation or by a system of equations (e.g., the linearized Euler equations). In this work, the scalar equation approach is chosen because an analytical solution for the radiated sound field is sought.

The scalar equations were pioneered by Lighthill,<sup>1</sup> who, by rewriting the governing equations, derived

$$\frac{\partial^2 \rho}{\partial t^2} - a_\infty^2 \frac{\partial^2 \rho}{\partial x_i^2} = \frac{\partial^2 T_{ij}}{\partial x_i \partial x_j} \quad (1)$$

where  $T_{ij} = \rho u_i u_j - \tau_{ij} + (p - a_\infty^2 \rho) \delta_{ij}$  and  $a_\infty$  is the ambient speed of sound. Equation (1) can be viewed as a wave equation for the propagation of sound. Several others have proposed scalar wave equations hence. Among others, the contributions by Phillips,<sup>2</sup> Lilley,<sup>3</sup> and Doak<sup>4</sup> can be mentioned. Curle<sup>5</sup> solved Lighthill’s equation on a bounded domain, and Ffowcs Williams and Hawkings<sup>6</sup> extended Curle’s solution to include surfaces in motion. The present work focuses on problems involving solid surfaces, but where the surfaces are stationary relative to the observer. For such problems, the solutions by Curle and Ffowcs Williams and Hawkings are equivalent, and it is matter of preference which one to use. Here, Curle’s equation will be used.

When working with the scalar acoustic equations, it is vital to understand the assumptions introduced. In the case of Lighthill’s equation, no assumptions have been made in the derivation, and hence it is exact. When solving Lighthill’s equation analytically, however, it is implicitly assumed that the source terms do not depend on the acoustic field, and that the isotropic wave operator describes the propagation of sound correctly. Mathematically speaking, the first assumption is never true because the density appears on both sides of the equation, as pointed out by for example Doak.<sup>4</sup> Physically speaking, it can be argued that the first assumption is a valid one (i.e., that it introduces only small errors) when the sound is generated by hydrodynamic phenomena, which are almost independent of the acoustic field. The second assumption is true only in regions where the fluid is stagnant. In low-Mach-number flows, the second

Received 20 March 2003; presented as Paper 2003-3237 at the AIAA/CEAS 9th Aeroacoustics Conference, Hilton Head, SC, 12–14 May 2003; revision received 24 February 2004; accepted for publication 30 June 2004. Copyright © 2004 by Johan Larsson. Published by the American Institute of Aeronautics and Astronautics, Inc., with permission. Copies of this paper may be made for personal or internal use, on condition that the copier pay the \$10.00 per-copy fee to the Copyright Clearance Center, Inc., 222 Rosewood Drive, Danvers, MA 01923; include the code 0001-1452/04 \$10.00 in correspondence with the CCC.

\*CFD Engineer, Fluid Dynamics Centre; also Ph.D. Student, Division of Thermo and Fluid Dynamics, Chalmers University of Technology, S-41296 Göteborg, Sweden; currently Ph.D. Student, Department of Mechanical Engineering, University of Waterloo, 200 University Avenue West, Waterloo, ON N2L 3G1, Canada; njlarso@sunwise.uwaterloo.ca.

†Professor, Division of Thermo and Fluid Dynamics; lada@tf.d.chalmers.se.

‡Manager, CFD Group, Fluid Dynamics Centre.

§Professor, Division of Thermo and Fluid Dynamics.

assumption is expected to be a good approximation because convection effects are a factor  $M$  slower than the propagation of the acoustic waves. A more thorough discussion can be found in Larsson.<sup>7</sup>

### A. Objectives

The objectives of the present work are to 1) investigate the noise generation process, specifically the noise generation in wall-bounded, separated, low-Mach-number flows; 2) derive a form of the solution to Lighthill's equation that is suitable for the computational applications of interest and valid in both the near and far fields; and 3) quantify the importance of the sound sources existing in the fluid, compared to that of the sources existing on solid walls.

### B. Open Cavity

The test case chosen in this study is the open cavity, which has been investigated theoretically experimentally, and computationally by many researchers. Although making no attempt at reviewing all of the work that has been done on the open cavity, included here is some that is relevant to the current work.

Gharib and Roshko<sup>8</sup> studied the incompressible flow in and around axisymmetric cavities experimentally and found that the flow in a cavity is heavily dependent on the length to depth  $L/D$  ratio. At low  $L/D$ , a shear layer is formed along the upper part of the cavity. The flow above the cavity is relatively undisturbed, and the main unsteady flow feature is the convection of vortices in the shear layer. The drag of the cavity is fairly low, typically  $C_D \sim 0.01$ . At higher  $L/D$ , the flow becomes more violent and unsteady. A vortex that fills the whole cavity is formed at the leading edge of the cavity, and when it is large enough it is released at the trailing edge. The flow above the cavity is affected by the flow inside the cavity, and freestream fluid is periodically directed into the cavity. The drag in this flow regime is much higher, typically  $C_D \sim 0.3$ . Gharib and Roshko used the term *wake-mode* to describe this latter flow regime, and some researchers use the term *shear-mode* to describe the first one. Here, the terms *shear regime* and *wake regime* will be used, in order to avoid confusion with the term *mode*, which is used for dominant frequencies.

The review of Rockwell and Naudascher<sup>9</sup> offers an excellent overview of the various types of cavity flows and of what parameters are important in determining the character of the flow. Included in this review are the measurements and findings by Ethembabaoglu,<sup>10</sup> Sarohia,<sup>11</sup> and Rossiter.<sup>12</sup> Ethembabaoglu performed incompressible experiments with turbulent boundary layers and found that the spectra of the wall-pressure fluctuations were highly organized with clear peaks. This suggests that a feedback mechanism is present, which couples the flow and the acoustics in a two-way manner (the feedback mechanism will be explained at the end of this section), and that the turbulence itself might be of secondary importance to the oscillations. In experiments with laminar boundary layers, Sarohia found that the influence of the cavity depth is insignificant, unless it is of the same order of magnitude as the boundary-layer thickness  $\delta_{0.99}$ . Rossiter stressed the importance of the boundary layer upstream of the cavity and found that a thinner boundary layer generates larger levels of fluctuations in the cavity.

Ahuja and Mendoza<sup>13</sup> performed aeroacoustic measurements in cavities with the purpose of using the results for validation of CAA codes. Among other things, they studied the importance of  $\delta_{0.99}$ ,  $L/D$  ratio, the influence of the spanwise width of the cavity, and the Mach number, on the radiated sound in several directions.

Especially during the past couple of years, several numerical studies of open cavity flows have been published. Rowley et al.<sup>14</sup> performed direct simulations of the flow in two-dimensional cavities at fairly low Reynolds numbers, typically  $Re_D = 1.5 \times 10^3$ . Varying several parameters, including  $L/D$ ,  $M$ , and  $\delta_{0.99}$ , they found that the primary parameter deciding which flow regime (shear or wake regime) that will be present is  $L/\theta$ , where  $\theta$  is the momentum thickness of the boundary layer.

Shieh and Morris<sup>15</sup> performed detached eddy simulations of cavities with  $L/D = 2$  and  $4.4$  at Mach numbers  $0.4$ ,  $0.5$ , and  $0.6$ . Their presented Reynolds number is  $2 \times 10^5$ , but it is unclear from their paper on what dimension this is based. They found that the mean

streamlines in the shear regime are virtually undisturbed above the cavity but clearly not so in the wake regime. Also, they found the mean pressure profiles along the bottom of the cavity to be distinctly different between the shear and wake regimes.

Ashcroft and Zhang<sup>16</sup> repeated Ahuja and Mendoza's measurements using unsteady Reynolds-averaged Navier–Stokes and were able to capture the main flow features. This is yet another indication that it is the feedback mechanisms of the low-frequency modes that are controlling the cavity flow.

Many attempts at deriving feedback models that predict the dominant frequencies have been made, with Rossiter's<sup>12</sup> being the first one. These models typically try to model the convection of a vortex in the shear layer, the impingement of this vortex on the downstream cavity wall, the propagation upstream of an acoustic wave, and the triggering of a new vortex near the leading edge. These models are typically fairly successful in predicting shear regime flows, but rather unsuccessful in predicting wake regime flows. This comes as no surprise, because the feedback mechanism modeled only applies to the shear regime. The current focus of feedback modeling seems to be to find the criterion for the regime switching. Rossiter's model is

$$Sr_L = fL/U_\infty = (m - \phi)/(M + 1/\kappa) \quad (2)$$

where  $f$  is the frequency,  $m$  is the mode number (integer),  $\phi$  is the phase lag between vortex impingement and emission of sound at the downstream wall, and  $\kappa$  is the ratio of the eddy convection velocity to the freestream velocity.

The case studied in the current work has a length to depth ratio of  $L/D = 4$ , a Mach number of  $M = 0.15$ , and a Reynolds number of  $Re_D = 1.5 \times 10^3$ . At this Reynolds number, the flow is laminar. The incoming boundary-layer thickness is chosen to ensure wake regime flow because the more violent flow in this regime is more representative of the separated flows that are of interest.

Because no experimental or computational data exist for this particular case, a direct simulation (DS) that resolves both the flow and the acoustics is performed. The term direct simulation is used here to avoid confusion with direct numerical simulation, a term normally used for the simulation of turbulence. The DS will be used to compute the source terms in Curle's integral solution and will be used for the purpose of comparisons. Because of the high cost of the DS, it is carried out in two dimensions.

## II. Methodology, Direct Simulation

The code used for the direct simulation is based on the finite volume code written by Eriksson.<sup>17</sup> Versions of this code have previously been used to study jet noise<sup>18</sup> and the sound emitted from shear layers.<sup>19</sup> Several modifications were made, including increasing the spatial and temporal accuracy, making the code work in two dimensions, and making the code parallel by the use of message passing interface. The modifications are described in greater detail in Larsson.<sup>7</sup>

### A. Governing Equations

The compressible Navier–Stokes equations, written on a compact, conservative form, are

$$\frac{\partial Q}{\partial t} + \frac{\partial E_j}{\partial x_j} = \frac{\partial F_j}{\partial x_j} \quad (3)$$

where  $Q = (\rho, \rho u_i, \rho e_0)^T$  is the state vector,  $E_j = (\rho u_j, \rho u_i u_j + p \delta_{ij}, \rho e_0 u_j + p u_j)^T$  are the inviscid fluxes, and  $F_j = (0, \tau_{ij}, \tau_{ij} u_i - q_j)^T$  are the viscous fluxes. The viscous stress tensor is

$$\tau_{ij} = \mu \left( \frac{\partial u_i}{\partial x_j} + \frac{\partial u_j}{\partial x_i} - \frac{2}{3} \frac{\partial u_k}{\partial x_k} \delta_{ij} \right) \quad (4)$$

and the heat flux  $q_i$  is modeled by Fourier's heat law

$$q_i = -\frac{c_p \mu}{Pr} \frac{\partial T}{\partial x_i} \quad (5)$$

where  $c_p$  is the specific heat at constant pressure. The total internal energy is  $e_0 = e + u_i u_i / 2$ .

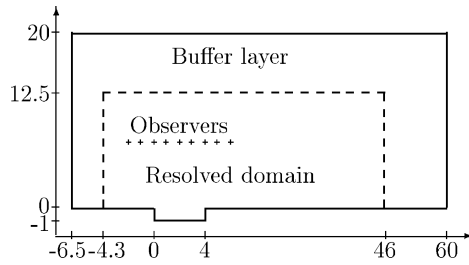


**Fig. 1** Computational domain, not to scale, coordinates normalized by  $D$ .

### B. Numerical Method

The governing equations are discretized using the finite volume method. The inviscid fluxes are computed by the dispersion-relation-preserving scheme of Tam and Webb.<sup>20</sup> The viscous fluxes, being orders of magnitude smaller than the inviscid ones in the major part of the domain and less important for the acoustics, are computed by a second-order-accurate, central scheme. The solution is stepped in time using a fourth-order-accurate, four-stage Runge–Kutta method.

The boundary conditions are based on the characteristic variables at the boundary and are similar to those developed by Thompson.<sup>21</sup> These boundary conditions are nonreflective only for disturbances normal to the boundary, but have been reported<sup>15,22</sup> to be robust for problems where large nonlinear fluctuations (vortices) have to leave the domain. To minimize the reflections from the boundaries, numerical buffer layers have been added. In the buffer layers, Eq. (3) is replaced by

$$\frac{\partial Q}{\partial t} + \frac{\partial E_j}{\partial x_j} = \frac{\partial F_j}{\partial x_j} - \sigma_0 \frac{a_\infty}{L_b} \xi^2 (Q - Q^*) \quad (6)$$

where  $\sigma_0$  is a buffer parameter,  $L_b$  is the length of the buffer layer,  $\xi$  is the nondimensional distance from the beginning of the buffer layer ( $0 \leq \xi \leq 1$ ), and  $Q^*$  is the target state. At the end of every time step, the field is also filtered in the buffer layers using a fourth-order filter similar to the one used by Colonius et al.,<sup>22</sup> where the filter strength is increased gradually throughout the buffer layers using the hyperbolic tangent function.

### C. Computational Grid

The computational domain is shown in Fig. 1, where the flow is from left to right. The resolution is roughly 80 cells per unit length  $D$  in and around the cavity, and the grid is stretched less than 1% per cell in the whole resolved domain. An upper limit on the cell size (roughly three times the smallest cell size) is set to avoid acoustic waves being reflected in the grid; if a high wave-number wave reaches a region where the cell size is too large for it to be resolved, it will be reflected in the grid and contaminate the solution. The resolved domain extends between  $-4.3 \leq x_1/D \leq 46$ , and  $x_2/D \leq 12.5$ . The total number of cells is 1,120,080, of which 287,460 are located in the buffer layers.

### D. Grid Independence

Grid-independence studies are important in all areas of computational fluid dynamics and especially so in direct simulations of sound. The resolution has to be fine enough to resolve all important physics, and the boundary conditions must not affect the solution significantly. The latter is critical in CAA because sound waves propagate over large distances. Although a boundary might be far away from the region of interest, any reflected sound waves will contaminate the solution in the whole domain.

The shortest wavelength of interest is  $\lambda_{\min}/D = (L/D)/(MSr_L) \approx 7$  because most of the energy is contained in  $Sr_L \leq 4$ . At this wavelength, the resolution is roughly 500 cells per wavelength, which indicates that the resolution is, indeed, fine.

The influence of the locations of the boundaries is tested by a simulation using a similar grid in and around the cavity, but with the boundaries moved farther away. The downstream boundary is moved  $12D$  to  $x_1/D = 58$ , and the freestream boundary is moved  $2.2D$  to  $x_2/D = 14.7$ . The lengths of the buffer layers and all buffer

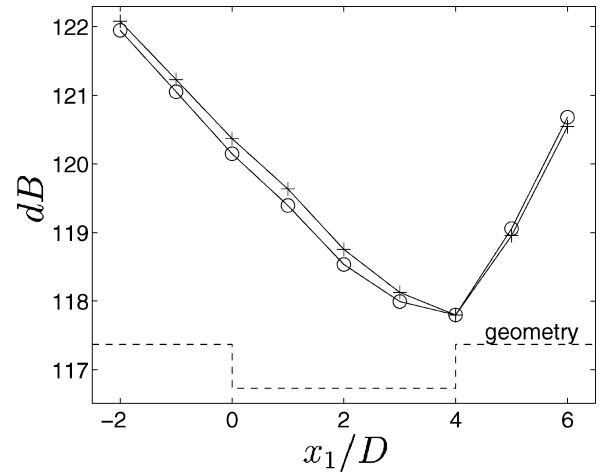


**Fig. 2** Grid independence, OASPL:  $\circ$ , standard grid and  $+$ , larger grid.

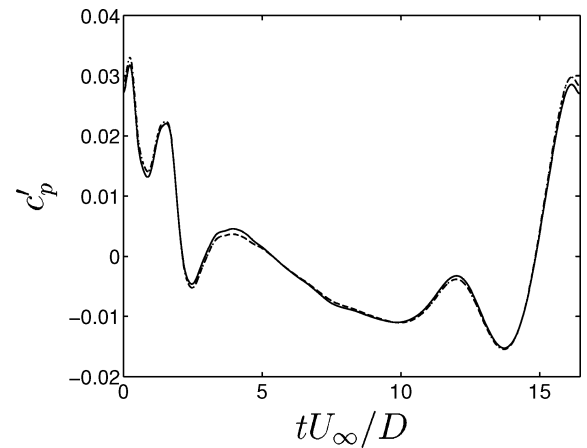


**Fig. 3** Grid independence,  $p'$  vs time: —, standard grid and — —, larger grid.

parameters are kept constant. The location of the upstream boundary is kept because it determines the incoming boundary layer.

The main parameters  $Sr_L$  and  $\tilde{C}_D$  are changed less than 0.2%, which is encouraging, but expected. The real test is the sound at the observer locations (shown in Fig. 1) because the boundary conditions can reflect or generate sound that would contaminate the sound at those (or any other) positions. The overall sound pressure level (OASPL) is computed for both the standard grid and the larger one and plotted in Fig. 2. The maximum difference between the two grids is 0.2 dB and occurs for the observers located at  $x_1/D \leq 2$ . The pressure signals from the two grids at location 4 ( $x_1/D = 1$ ) are plotted in Fig. 3 because this is the observer for which the maximum difference occurs. It is seen that there are only slight changes in amplitude at some times, and hence the solution is considered to be grid independent to within approximately 0.2 dB.

Pressure signals from within, or very close to, the cavity are much less sensitive to the location of the boundaries. In this case, the errors are almost two magnitudes lower for pressure signals at  $x_2/D = 0$ . This is because the flow in the cavity is largely governed by hydrodynamic phenomena, which are insensitive to reflections from the free boundaries.

## III. Methodology, Curle's Equation

Curle<sup>5</sup> wrote the solution to Lighthill's equation in three dimensions as

$$\rho(\mathbf{x}, t) - \rho_0 = \frac{1}{4\pi a_\infty^2} \frac{\partial^2}{\partial x_i \partial x_j} \int_V \frac{T_{ij}}{r} dV(\mathbf{y}) - \frac{1}{4\pi a_\infty^2} \frac{\partial}{\partial x_i} \int_S \frac{n_j}{r} (p\delta_{ij} - \tau_{ij}) dS(\mathbf{y}) \quad (7)$$

where  $\rho_0$  is a constant of integration,  $r = |\mathbf{x} - \mathbf{y}|$  is the distance between the source and the observer, and  $\mathbf{n}_j$  is the surface normal pointing toward the fluid. The integrands are to be evaluated at the retarded time  $\tau = t - r/a_\infty$ . Despite the fact that the present simulations are performed in two dimensions, the three-dimensional formulation of Curle's equation is used. The reason for this is simply convenience because the work will move to fully three-dimensional simulations later. Note that the two-dimensional equivalent to Eq. (7) (for example, see Gloerfelt et al.<sup>23</sup>) is exactly equivalent to Eq. (7) with the integral over the third dimension extending to infinity.

#### A. Modified Curle's Equation

For numerical implementations, it is convenient to rewrite Eq. (7) on a form where the derivatives are taken inside the integral.<sup>24</sup> Also, in the current simulations the resolution is higher in time than it is in space, and hence it is desirable to transform the spatial derivatives to temporal ones for purposes of accuracy.

If the observer in Eq. (7) is located in a region where the flow is isentropic, the density fluctuation at this location can be written  $\rho(\mathbf{x}, t) - \rho_0 = [p(\mathbf{x}, t) - p_0]/a_\infty^2$ . For a function  $f(\tau)$  the spatial derivative can be converted to a temporal one by

$$\frac{\partial f(\tau)}{\partial x_i} = \frac{\partial f}{\partial \tau} \frac{\partial \tau}{\partial x_i} = -\frac{1}{a_\infty} \frac{\partial r}{\partial x_i} \frac{\partial f}{\partial \tau} \quad (8)$$

The  $\partial r/\partial x_i$  term becomes

$$\frac{\partial r}{\partial x_i} = \frac{\partial \sqrt{(x_j - y_j)^2}}{\partial x_i} = \frac{(x_i - y_i)}{\sqrt{(x_j - y_j)^2}} = \frac{x_i - y_i}{r} = l_i \quad (9)$$

where  $l_i$  is a unit vector pointing from the source location to the observer location. Using this, Eq. (7) can be written as

$$\begin{aligned} p(\mathbf{x}, t) - p_0 &= \frac{1}{4\pi} \frac{\partial}{\partial x_i} \int_V -l_j \left( \frac{\dot{T}_{ij}}{a_\infty r} + \frac{T_{ij}}{r^2} \right) dV(\mathbf{y}) \\ &\quad - \frac{1}{4\pi} \int_S -l_i n_j \left( \frac{\dot{p}\delta_{ij} - \dot{\tau}_{ij}}{a_\infty r} + \frac{p\delta_{ij} - \tau_{ij}}{r^2} \right) dS(\mathbf{y}) \\ &= \frac{1}{4\pi} \int_V \left[ l_i l_j \left( \frac{\ddot{T}_{ij}}{a_\infty^2 r} + 2 \frac{\dot{T}_{ij}}{a_\infty r^2} + 2 \frac{T_{ij}}{r^3} \right) \right. \\ &\quad \left. - \frac{\partial l_j}{\partial x_i} \left( \frac{\dot{T}_{ij}}{a_\infty r} + \frac{T_{ij}}{r^2} \right) \right] dV(\mathbf{y}) \\ &\quad + \frac{1}{4\pi} \int_S l_i n_j \left( \frac{\dot{p}\delta_{ij} - \dot{\tau}_{ij}}{a_\infty r} + \frac{p\delta_{ij} - \tau_{ij}}{r^2} \right) dS(\mathbf{y}) \end{aligned} \quad (10)$$

The term  $\partial l_j/\partial x_i$  is expanded to

$$\frac{\partial l_j}{\partial x_i} = \frac{\partial}{\partial x_i} \left( \frac{x_j - y_j}{r} \right) = \frac{\delta_{ij} - l_i l_j}{r} \quad (11)$$

Inserting this into Eq. (10) yields

$$\begin{aligned} p(\mathbf{x}, t) - p_0 &= \frac{1}{4\pi} \int_V \left( \frac{l_i l_j}{a_\infty^2 r} \ddot{T}_{ij} + \frac{3l_i l_j - \delta_{ij}}{a_\infty r^2} \dot{T}_{ij} \right. \\ &\quad \left. + \frac{3l_i l_j - \delta_{ij}}{r^3} T_{ij} \right) dV(\mathbf{y}) \\ &\quad + \frac{1}{4\pi} \int_S l_i n_j \left( \frac{\dot{p}\delta_{ij} - \dot{\tau}_{ij}}{a_\infty r} + \frac{p\delta_{ij} - \tau_{ij}}{r^2} \right) dS(\mathbf{y}) \end{aligned} \quad (12)$$

Equation (12) is similar to formulations by for example Brentner and Farassat<sup>24</sup> and is well suited for the present simulations. The first term in each integral has a  $1/r$  dependence and will survive into the far field, whereas the terms with  $1/r^2$  or  $1/r^3$  dependencies are near-field terms.

The integrals in Eq. (12) should be taken over all space and all solid walls, respectively. This is of course impossible in practical applications, so that instead the integrals need to be taken over a large enough region to ensure that they have converged. This will be investigated in Sec. V.B.

#### B. Extension in the Third Direction

When using the three-dimensional formulation of Curle's equation, the integral has to be taken to infinity in the third dimension. Because this is exactly equivalent to using a two-dimensional analog of Eq. (12) and because this two-dimensional analog exists and is well defined, it is known a priori that the integral to infinity will be convergent. In practice, the bounds in the third dimension are not infinity, but rather large enough to ensure that the error involved is smaller than all other errors (less than 1%). In the current case two-dimensional flow is assumed, and hence the two-dimensional field is assumed to be identical at all locations in the third dimension.

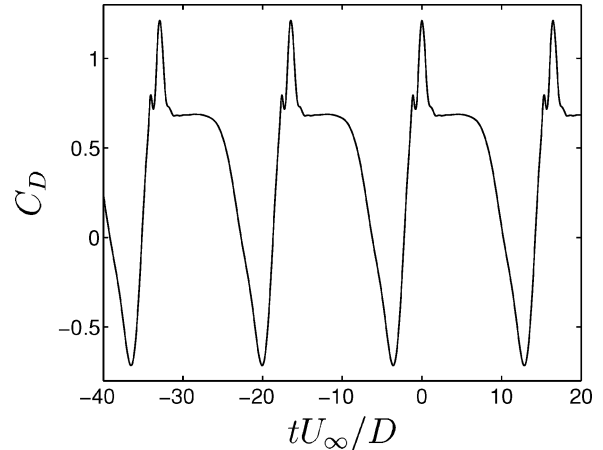
### IV. Results: Flowfield

#### A. Cavity Drag

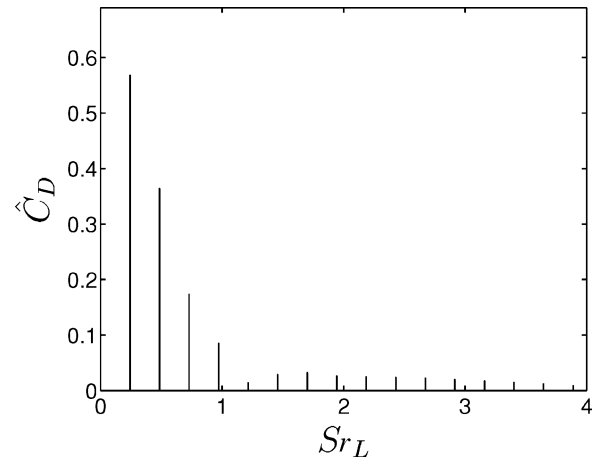
The drag of the cavity per unit width (being a two-dimensional geometry) is defined as

$$C_D = F_1 / \frac{1}{2} \rho_\infty U_\infty^2 D \quad (13)$$

where  $F_1$  is the force per unit width in the  $x_1$  direction. After the initial transients have disappeared, a statistically stationary state is reached, as can be seen in Fig. 4a. The mean drag is  $\bar{C}_D = 0.377$ , and the drag associated with pressure alone (no viscous stress) is  $\bar{C}_D^p = 0.402$ , that is, larger than the total drag. This is because the flow along the bottom of the cavity is mainly toward the left, and



a)  $C_D$  vs time



b)  $C_D$  spectrum

Fig. 4 Cavity drag.

hence the viscous contribution is actually to lower the drag. The values computed in this study are in qualitative agreement with other published results. Gharib and Roshko<sup>8</sup> report  $\bar{C}_D \sim 0.3$  for the incompressible flow in axisymmetric cavities. Rowley et al.<sup>14</sup> report  $\bar{C}_D = 0.227$  for a similar case but at  $M = 0.6$ .

The spectrum of the cavity drag is plotted in Fig. 4b, where the amplitude  $\hat{C}_D$  of the drag is plotted vs the Strouhal number defined by

$$Sr_L = fL/U_\infty \tag{14}$$

The fundamental frequency is  $Sr_L = 0.243$ , and all higher modes are harmonics of this fundamental frequency. The first four modes are the largest, which means that most of the energy resides at  $Sr_L \leq 1$ . The results compare favorably with other published results. Rowley et al.<sup>14</sup> report a fundamental frequency  $Sr_L = 0.256$ , which is very close to the value computed here. Other results worth mentioning are the ones by Ethembabaoglu,<sup>10</sup> who got  $Sr_L \approx 0.5$  for the incompressible turbulent flow in a cavity with  $L/D = 4$ , and Shieh and Morris,<sup>15</sup> who got  $Sr_L = 0.216$  in a cavity with  $L/D = 4.4$  for  $M = 0.6$  and turbulent flow.

**B. Incoming Boundary Layer**

Most studies on open cavity flows show the importance of the incoming boundary layer (BL), but few study it in more detail. An attempt at doing this is included here. Because the incoming BL in this study is laminar, the famous Blasius solution (for example, see White<sup>25</sup>) is available for flat-plate flows. Comparisons between the time-averaged BL in the simulation and the analytical solutions for a flat plate can yield some insight into open cavity flows.

The momentum thickness  $\theta$  at the beginning of the resolved domain ( $x_1/D = -4.3$ ) is used to compute the virtual origin of the BL, and this virtual origin is then used to determine the analytical solutions of the boundary-layer parameters.<sup>25</sup>

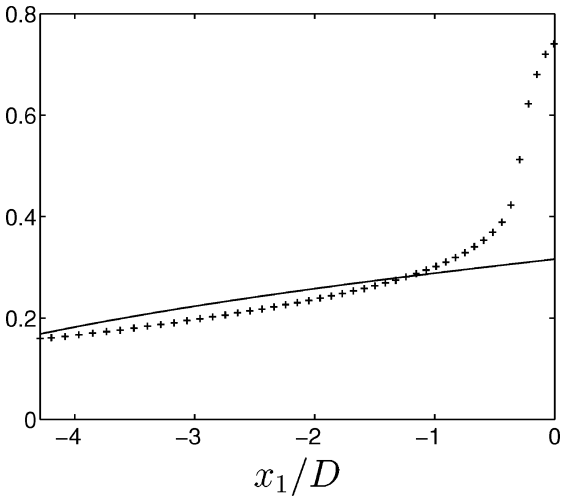
The computed BL parameters are plotted in Fig. 5 together with the analytical solutions for a flat plate. It is seen that the time-averaged BL behaves in a very different way compared to a flat-plate BL. The growth rate increases downstream, instead of decreasing like the flat-plate solution. The plot of the momentum thickness is especially disturbing; because  $\theta(x_1)$  is a measure of the drag from the virtual origin to  $x_1$ , Fig. 5b suggests that the plate drag up to  $x_1/D \approx -3.7$  is negative, which it of course cannot be. The problem here is that all of these theories are based on a uniform freestream velocity  $U_\infty$ , but the freestream velocity is actually increasing slowly with  $x_1$  in this case. The reason is the periodic buildup and shedding of a vortex, which forces the freestream to accelerate around it.

From Fig. 5, it is seen that the boundary layer is affected by the presence of the cavity quite far upstream, in fact all of the way to the buffer layer. This indicates that the inlet needs to be placed relatively far away from the cavity when wake regime oscillations are of interest.

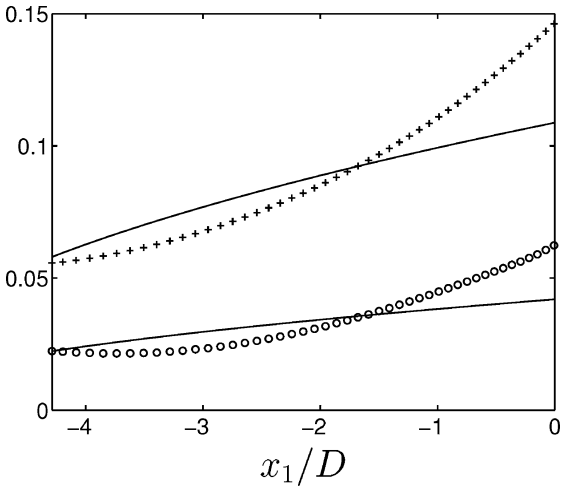
The fact that the incoming BL behaves as it does complicates comparisons with other published investigations. Colonius et al.,<sup>26</sup> for example, present the projected value of  $\theta$  at the leading edge, assuming laminar growth. Other researchers, especially the experimentalists, present time-averaged values of  $\delta_{0.99}$ ,  $\delta^*$ , or  $\theta$  at the leading edge. From the figures, it is clear that these measures can not be compared directly. The choice of Colonius et al. is specifically cumbersome because the projected values depend on how far upstream they are computed from. In this study, the projected and the actual parameters of the incoming BL are given in Table 1.

**Table 1 Incoming boundary-layer parameters at  $x_1 = 0$**

Parameter	Actual value	Projected value
$\delta_{0.99}/D$	0.741	0.316
$\delta^*/D$	0.146	0.109
$\theta/D$	0.0624	0.0419
$H$	2.34	2.59



**a) Boundary-layer thickness  $\delta_{0.99}/D$**



**b) +, Displacement thickness  $\delta^*/D$  and o, momentum thickness  $\theta/D$**

**Fig. 5 Incoming boundary layer: —, analytical solutions.**

**C. Flow Features**

The flow in open cavities is truly fascinating, with many complicated flow patterns despite the geometric simplicity. A sequence of snapshots with instantaneous streamlines are shown in Fig. 6. The time has been defined to be  $t \equiv 0$  at the peak in  $C_D$  (Fig. 4a).

Starting at  $tU_\infty/D = 12.35$ , a vortex is formed at the leading edge. This vortex grows, and at  $tU_\infty/D = 0$  a secondary vortex appears at the lower corner of the upstream cavity wall. At  $tU_\infty/D = 2.06$ , the primary vortex is large enough to deflect the flow above the cavity, and the boundary layer upstream of the cavity separates (albeit hard to see in the figures). At  $tU_\infty/D = 8.23$ , the secondary vortex (rotating counterclockwise) has grown large enough to reattach the upstream BL. At this time, the primary vortex has started to move downstream. At  $tU_\infty/D = 10.29$ , the primary vortex impinges on the downstream cavity wall, and during the next two snapshots it is ejected at the trailing edge. Freestream fluid is pulled down into the cavity at  $tU_\infty/D = 14.40$ , and it impinges on the downstream cavity wall at  $tU_\infty/D = 0$ , which is when the maximum drag occurs. The ejected vortices are convected along the wall downstream of the cavity until they leave the resolved domain.

A sequence of snapshots of the instantaneous vorticity downstream of the cavity is shown in Fig. 7. The large vortices rotating in the clockwise direction (negative vorticity, solid lines) located roughly  $5D$  apart are the two vortices seen leaving the cavity in Fig. 6. These vortices move downstream at a fairly constant velocity of about  $0.6U_\infty$ . In addition, there are smaller vortices rotating counterclockwise (positive vorticity, dashed lines), which in general are located above the larger vortices. Being located farther away from the wall, these vortices travel at a higher velocity of

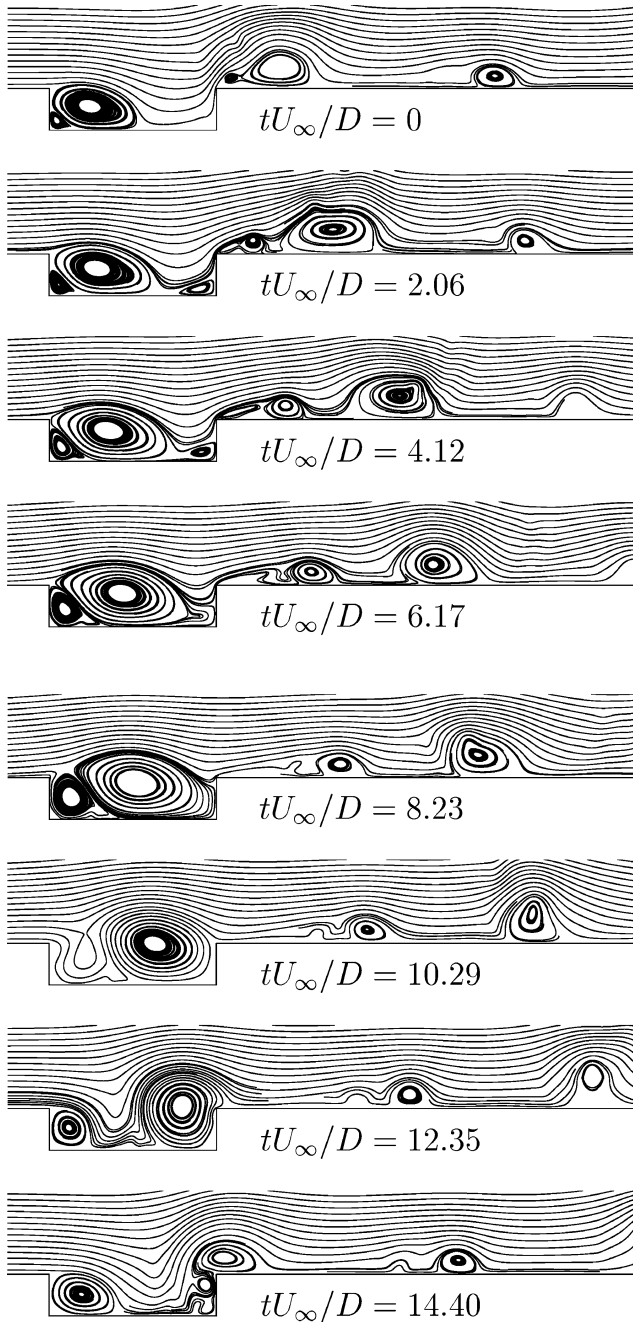


Fig. 6 Instantaneous streamlines:  $-1 < x_1/D < 14$ ,  $x_2/D < 2$ .

about  $0.9U_\infty$ . At  $x_1/D \approx 12$  (Fig. 7,  $tU_\infty/D = 12.35$ ),  $x_1/D \approx 21$  ( $tU_\infty/D = 0$ ), and  $x_1/D \approx 29$  ( $tU_\infty/D = 12.35$ ); the smaller counterclockwise rotating vortices overtake the larger clockwise rotating ones. As it overtakes the larger vortex, the smaller vortex is essentially swept along by the larger one. This increases the velocity of the counterclockwise rotating vortices momentarily, and hence their convection velocity is relatively unsteady.

The pressure coefficient  $c_p$  is defined as

$$c_p = \frac{p - p_\infty}{\frac{1}{2}\rho_\infty U_\infty^2} \quad (15)$$

The mean value  $\bar{c}_p$  is plotted in Fig. 8. The parameter  $s$  in the figure is the distance from the leading edge along the wall, and the vertical lines outline the corners of the cavity.

The mean pressure  $\bar{c}_p$  is low on the upstream cavity wall and in the beginning of the cavity. It rises steeply towards the end of the cavity and reaches a maximum in the lower, downstream wall, corner. This maximum is a result of the periodic impingement of freestream fluid,

which creates a stagnated region. The pressure decreases sharply at the trailing edge because of the high acceleration around the edge. Behind the cavity, the pressure rises slowly and reaches a small peak at  $x_1/D \approx 12$  (i.e.,  $s/D \approx 14$ ), from where it falls off.

The  $\bar{c}_p$  along the bottom wall from Shieh and Morris<sup>15</sup> is included in Fig. 8. Despite being a different case ( $L/D = 4.4$ ,  $M = 0.6$ ,  $Re = 2 \times 10^5$ ,  $\delta_{0.99}/D = 0.2$ ), the mean pressure coefficients are remarkably similar. Note that their results were for a longer cavity, and hence their bottom wall extends to  $s/D = 5.4$ . The trends are very similar: a minimum at  $x_1/D \approx 1$  followed by a steep increase as the downstream cavity wall is approached. Shieh and Morris got a larger maximum value of  $\bar{c}_p$  at the downstream cavity wall, which could be a result of their longer cavity, giving the flow a larger distance for pressure recovery. This hypothesis is strengthened by the fact that the profiles follow the same trend between  $x_1/D \approx 2$  and  $x_1/D \approx 3.5$ . Another possibility is that the higher Mach number of Shieh and Morris's case gives higher oscillations, an idea that is emboldened by the fact that all peaks are stronger in their results. A last possibility is the fact that their results were computed using a turbulence model, which could have given erroneous results.

The small peak of  $\bar{c}_p$  at  $x_1/D \approx 12$  is probably an effect of a small counterclockwise rotating vortex. This smaller vortex is only seen in Fig. 6 as a small disturbance of the larger vortex as it travels downstream from the cavity. At  $x_1/D \approx 12$  ( $s/D \approx 14$ ), the smaller vortex is located in the lower part of the primary vortex, and this can enhance the entrainment of fluid towards the wall. This would then increase the pressure on the wall at that location.

## V. Results: Radiated Sound

One of the objectives listed in Sec. I.A is to analyze the acoustic noise generation in detail, which is an area that has received remarkably little attention, at least in computational studies, judging from published work. Among the few investigations dealing in detail with the sources of sound, Freund's<sup>27</sup> study of the noise sources in a jet and Mankbadi et al.'s<sup>28</sup> investigation of supersonic jet noise are two examples.

At the outset, the sound sources are highly nonlocal at this low Mach number, and hence observations regarding the location of important sound sources are weak, whereas observations regarding the relative strengths of different source terms are stronger. Nevertheless, it is still of interest to see where the sound sources are large because this yields insight into the sound generation process.

### A. Contributing Source Terms

From Lighthill's theory it is possible to deduce scaling laws for the intensity of different types of sound sources (for example, see Crighton<sup>29</sup>). One consequence of these scaling laws is that the pressure fluctuations on solid walls will be the primary sources of sound at low Mach numbers. Lighthill<sup>1</sup> also shows that  $T_{ij} \approx \rho_\infty u_i u_j$  for most flows at low Mach numbers. Because Curle's equation is linear, it is possible to compute the contributions from the various source terms independently and compare their relative magnitudes. It is then possible to quantify, for example, how dominant the surface-pressure fluctuations are in generating sound (for this particular flow).

Curle's equation in its modified form (12) involves a total of 13 source terms: nine in the volume [ $\dot{T}_{ij}$ ,  $T_{ij}$ , and  $T_{ij}$ , where each consists of  $\rho u_i u_j$ ,  $\tau_{ij}$ , and  $(p - a_\infty^2 \rho) \delta_{ij}$ ] and four on the walls ( $\dot{p}$ ,  $\dot{\tau}_{ij}$ ,  $p$ , and  $\tau_{ij}$ ). Furthermore, because the common simplification of  $T_{ij}$  introduces  $\rho_\infty$  Lighthill's tensor is best written (for purposes of comparing magnitudes)  $T_{ij} = \rho_\infty u_i u_j + (\rho - \rho_\infty) u_i u_j - \tau_{ij} + (p - a_\infty^2 \rho) \delta_{ij}$ , bringing the total number of source terms to 16.

To analyze the contribution of each source term, the radiated sound at an observer located at  $\mathbf{x}/D = (1, 7.16)$  is computed by Curle's equation. The sound intensity of each contribution is then computed by the far-field approximation<sup>30</sup>

$$\bar{I} = \overline{(p')^2} / \rho_\infty a_\infty \quad (16)$$

The use of the far-field approximation is strictly not valid, but is necessitated by the fact that Curle's equation only provides the fluctuating pressure.

The results, scaled with the intensity computed at the same observer from the DS, are presented in Table 2. As can be seen, the viscous terms (terms 3, 4, and 7) are negligible, both on the walls and in the volume. The assumption of  $\rho \approx \rho_\infty$  introduces a very small error (term 6), and the entropy term (term 8) is negligible as well. Because of these findings, the first- and zeroth-order temporal derivatives of the viscous, entropy, and  $(\rho - \rho_\infty)u_i u_j$  terms are skipped and not included in the table.

The contributions of the volume terms (terms 5, 9, and 10) are about 5% of the wall term contributions (terms 1 and 2). A comparison like this one, however, does not take any cancellation effects into account (i.e., it ignores phase information). To analyze the contributions further, the pressure signals are plotted vs time in Fig. 9.

Figure 9a shows the contributions of terms 1 and 2, as well as the sum of them. Note that some signals have been offset (moved down) slightly for clarity. The sum is very promising because it shows remarkable similarity to the signal computed in the DS. From the individual contributions, it is seen that terms 1 and 2 are roughly equally important (as indicated in Table 2), and that there exists a phase lag between terms 1 and 2 at the main peaks.

Figure 9b shows the total contribution of both wall and volume terms. When compared to the results from the wall terms alone, the agreement between the signals computed by Curle's equation and the DS is better around  $tU_\infty/D \approx 4$ , but worse around  $tU_\infty/D \approx 16$ .

**Table 2** Contributions from different source terms

Number	Term	$\bar{I}/\bar{I}_{DS}$
1	$\partial p / \partial \tau _w$	0.38
2	$p _w$	0.33
3	$\partial \tau_{ij} / \partial \tau _w$	$\sim 10^{-5}$
4	$\tau_{ij} _w$	$\sim 10^{-5}$
5	$\partial^2 \rho_\infty u_i u_j / \partial \tau^2$	0.0093
6	$\partial^2 (\rho - \rho_\infty) u_i u_j / \partial \tau^2$	$\sim 10^{-5}$
7	$\partial^2 \tau_{ij} / \partial \tau^2$	$\sim 10^{-5}$
8	$\partial^2 (p - a_\infty^2 \rho) \delta_{ij} / \partial \tau^2$	$\sim 10^{-4}$
9	$\partial \rho_\infty u_i u_j / \partial \tau$	0.025
10	$\rho_\infty u_i u_j$	0.027

So which terms are important in Curle's equation? The wall-pressure terms (1 and 2) are dominant and account for most of the radiated sound, whereas the simplified volume terms (5, 9, and 10) only modify the signal slightly. Whether the volume terms are important in terms of the radiated intensity will be analyzed in Sec. V.C.

## B. Convergence of the Curle Integral

As mentioned in Sec. III.A, the upper and lower limits (in the  $x_1$  and  $x_2$  directions; the  $x_3$  direction was dealt with in Sec. III.B) when computing Curle's integrals need to be located far enough away as to ensure convergence of the integrals. Because the wall-pressure source terms were found to be dominant, only this integral is considered here. Also, because the incoming boundary layer is laminar the upstream limit is not expected to be critical. Hence, only the effect of the downstream limit is investigated.

In simplified notation, the pressure signal

$$p_{1,2}(\mathbf{x}, t) - p_0 = \frac{1}{4\pi} \int_{S: x_1 < x_{1,d}} l_i n_j \left( \frac{\dot{p} \delta_{ij}}{a_\infty r} + \frac{p \delta_{ij}}{r^2} \right) dS(\mathbf{y}) \quad (17)$$

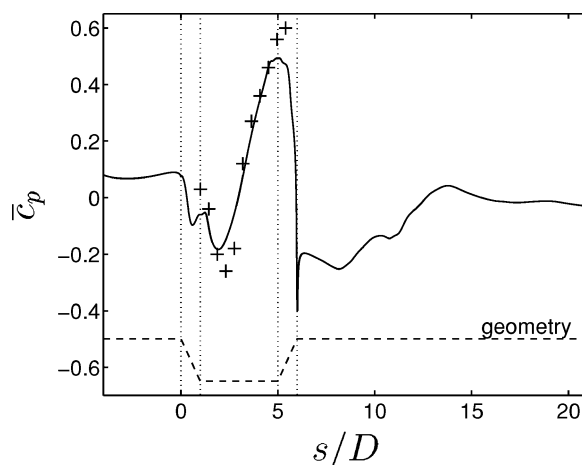


**Fig. 8** Mean pressure coefficient: —, DS and +, Shieh and Morris.<sup>15</sup>

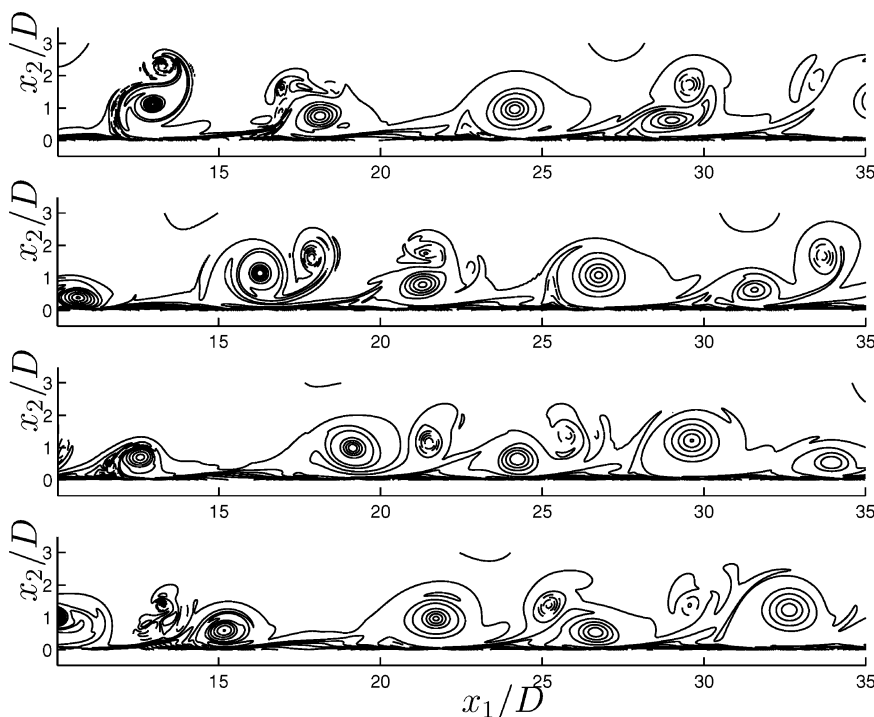
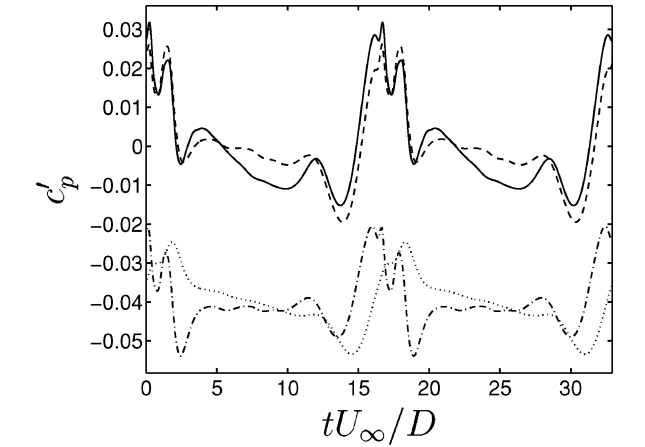
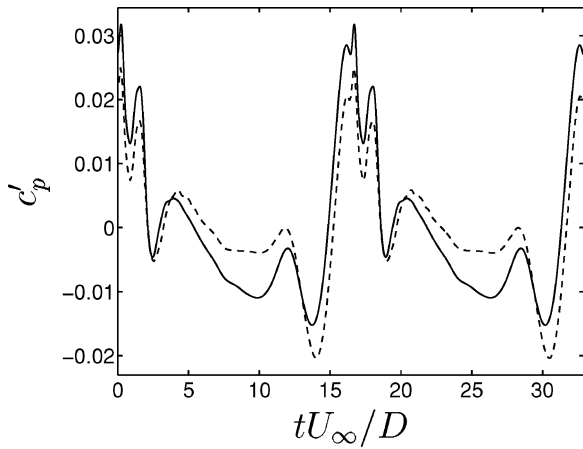


**Fig. 7** Instantaneous vorticity contours at times  $tU_\infty/D = 12.35, 0, 4.12$ , and  $8.23$ : —, negative and ---, positive contours.



a) —, DS; --, term 1 + 2; —·—, term 1 (offset  $-0.04$ ); ···, term 2 (offset  $-0.04$ )



b) —, DS; --, term 1 + 2 + 5 + 9 + 10

Fig. 9 Radiated pressure signals at  $x/D = (1, 7.16)$ .

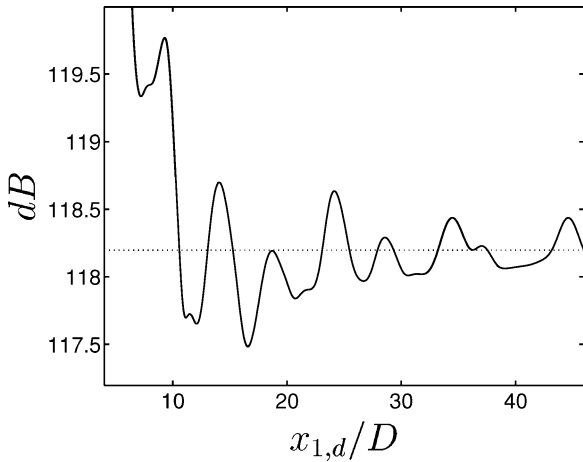


Fig. 10 Convergence of OASPL from Curle's integral for wall-pressure sources; observer located at  $x/D = (1, 7.16)$ .

is computed for  $x/D = (1, 7.16)$  and different downstream limits  $x_{1,d}$ . The OASPL [Eq. (18)] as a function of  $x_{1,d}$  is plotted in Fig. 10, and it is seen that even for the large domain used here the integral only converges to within approximately 0.2 dB. Because this is the same level as the estimated error from the grid resolution study, Curle's equation is considered converged to an acceptable level.

Aside from whether the integral has converged to accurate levels, Fig. 10 yields some insight into the locality of the sources. The fact that they are nonlocal is seen from the fact that the integral converges only slowly with  $x_{1,d}$  because the sources are correlated

Table 3 Observer locations

Observer	$x_1/D$	$x_2/D$
1	-2	7.16
2	-1	7.16
3	0	7.16
4	1	7.16
5	2	7.16
6	3	7.16
7	4	7.16
8	5	7.16
9	6	7.16

over large distances. On the other hand, the fact that inclusion of the source terms past  $x_1 \approx 10$  only changes the radiated sound by small amounts suggests that despite the nonlocality of the sources, the sources close to the cavity are dominant and account for most of the sound. The coherence of the sources can also be seen, in that the contributions from  $4 < x_1/D < 10$  essentially act to decrease the radiated intensity (for this particular observer). These sources must then be out of phase with the sources inside the cavity.

### C. Radiated Sound

The radiated sound to the observers, listed in Table 3 (see also Fig. 1), is computed by Curle's modified Eq. (12). Because only the fluctuating pressure is available from Curle's equation, the far-field approximation of the OASPL

$$\text{OASPL} = 10 \log_{10}(\bar{I}/I_{\text{ref}}) = 20 \log_{10}(p_{\text{rms}}/p_{\text{ref}}) \quad (18)$$

with  $p_{\text{ref}} = \sqrt{(\rho_{\infty} a_{\infty} I_{\text{ref}})}$  and  $I_{\text{ref}} = 10^{-12} \text{ W/m}^2$  is used. The OASPL from the wall-pressure contribution in Curle's equation is plotted in Fig. 11a, and it is seen that the levels are underpredicted by between 0.3 and 4.3 dB. The shape of the radiated OASPL is in fairly good agreement with the DS, but the underprediction is larger above the downstream wall. The reason to this is not known, but it is hypothesized that it might be caused by the lack of mean flow convection (which would enhance the downstream radiation). Looking at the individual contributions, the  $p/r^2$  part (term 2) shows the largest difference between different observers. Because this term disappears in the far field, the far-field directivity is expected to be flatter.

The radiated sound intensity when the volume terms are added is plotted in Fig. 11b. Addition of term 5 changes little. The full contribution, including all dominant wall and volume terms, has a similar maximum underprediction as the two wall terms alone, but the shape of the curve is in less qualitative agreement with that of the DS.

## VI. Acoustic Source Terms

The strength of the acoustic sources is defined here as

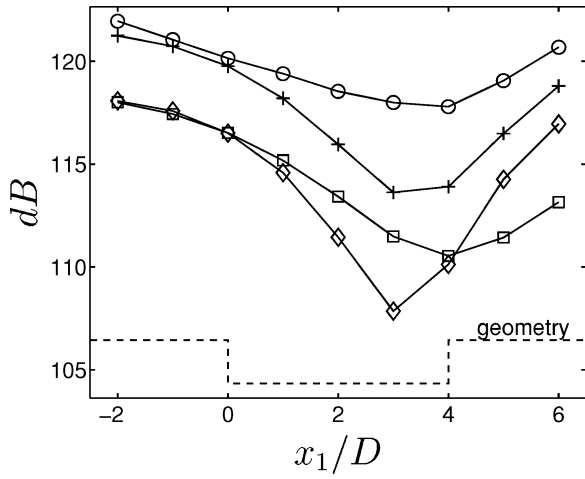
$$S_l \equiv 20 \log_{10}(\Phi_{l,\text{rms}}/\Phi_{l,\text{ref}}) \quad (19)$$

where  $\Phi_l$  is one of the source terms listed in Table 2. With this scaling, an increase of 10 dB is equivalent to a 10-fold increase in intensity, and an increase of 3 dB means a doubling of the intensity.  $\Phi_{l,\text{ref}}$  acts only to change the level of the source strength, and so, as long as only relative information is of interest, it can be chosen arbitrarily. Here, the reference for the wall-pressure fluctuation ( $l = 2$ ) is chosen to be the same as that for the OASPL of the radiated sound, that is,  $\Phi_{2,\text{ref}} = p_{\text{ref}} = \sqrt{(\rho_{\infty} a_{\infty} 10^{-12} \text{ W/m}^2)}$ . This choice means that  $S_2$  is the OASPL at the wall. Because some terms involve temporal derivatives, a factor  $U_{\infty}/D$  is included in  $\Phi_{l,\text{ref}}$  as, for example,  $\Phi_{1,\text{ref}} = p_{\text{ref}} U_{\infty}/D$ .

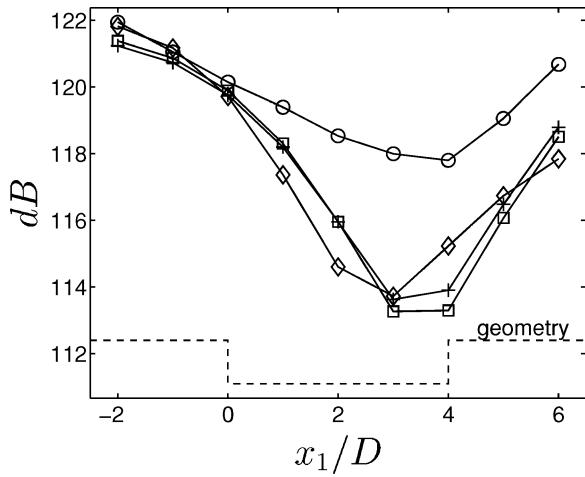
### A. Pressure Sources

The strengths of the wall pressure sources ( $S_1$  and  $S_2$ ) are plotted in Fig. 12a. They are small at the inlet and grow about a factor of 10 as they approach the leading edge. The low levels at the inlet are explained by the fact that the boundary layer is laminar, and the increase closer to the leading edge is caused by the periodic





a) ○, DS; +, term 1+2; □, term 1; ◇, term 2



b) ○, DS; +, term 1+2; □, term 1+2+5; ◇, term 1+2+5+9+10

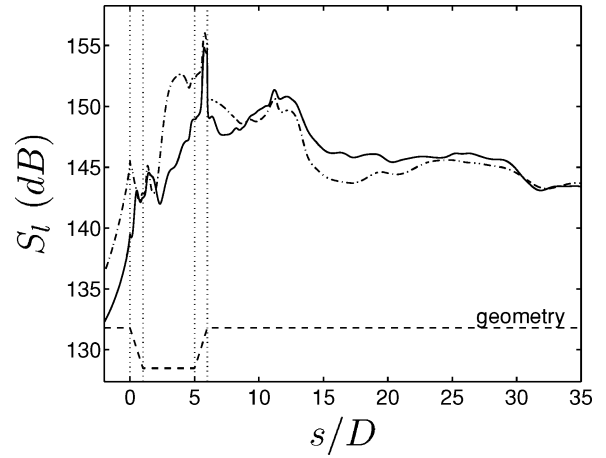
Fig. 11 Overall sound pressure levels at nine observers.

separation of the BL upstream of the leading edge. The sources grow even larger toward the end of the bottom cavity wall and reach a peak at the upper part of the downstream cavity wall. After the cavity, there is a small peak at  $x_1/D \approx 12$  (i.e.,  $s/D \approx 14$ ), behind which they drop about 5 dB. This drop occurs at the same location, where  $\bar{c}_p$  was found to have a small peak in Fig. 8 and where the small vortex was found in Fig. 6. There is a second drop in source strength at  $x_1/D \approx 29$ . Considering Fig. 7, it is interesting to note that the two drops in source strength coincide with the locations where the strongest counterclockwise rotating vortex overtakes a larger clockwise rotating vortex.

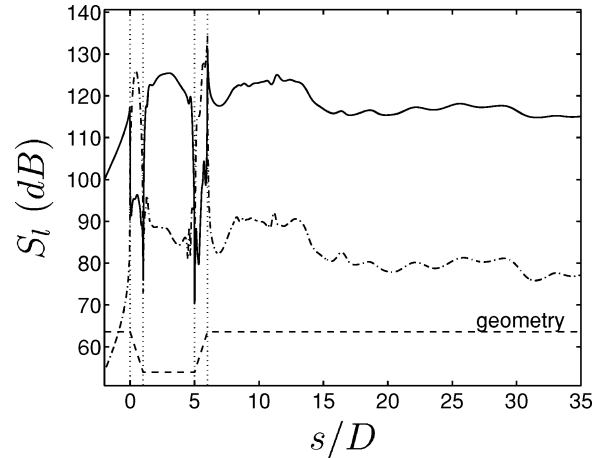
Source term 1 (i.e.,  $\bar{p}$ ) is Fourier transformed, and the strengths of the first four modes are plotted in Fig. 13. Modes 2 and 4 are dominant behind the cavity, and they both have peaks and subsequent drops at  $x_1/D \approx 12$  and, to a lesser extent, at  $x_1/D \approx 29$ . It can then be hypothesized that the vortex interactions at these locations mainly affect modes 2 and 4. The fundamental frequency (mode 1) is strongest around  $1 < x_1 < 3$  but rather weak behind the cavity. This is somewhat surprising because mode 1 is the strongest at essentially all observer locations in the DS and in the radiated sound from Curle. [Neither is shown, but the spectra are similar to the spectrum of  $C_D$  (Fig. 4b).]

The fact that the contributions of terms 1 and 2 were found to be of similar magnitude in Sec. V.A is, of course, not a coincidence. Assuming that terms 1 and 2 are affected similarly by cancellations, the radiated intensities would scale as

$$\frac{\bar{I}_2}{\bar{I}_1} \sim \frac{(Ap'/r^2)^2}{[(A/a_\infty r)(\partial p/\partial \tau)]^2} \sim \frac{a_\infty^2 p_{\text{rms}}^2}{r^2 \dot{p}_{\text{rms}}^2} \quad (20)$$



a) Pressure terms: —,  $S_1$ ; ---,  $S_2$



b) Viscous terms: —,  $S_4 (n_j \tau_{1j})$ ; ---,  $S_4 (n_j \tau_{2j})$

Fig. 12 Wall source strengths.

where  $A$  is some sound radiating area. Equation (19) is used to write

$$p_{\text{rms}}^2 = p_{\text{ref}}^2 10^{S_2/10}, \quad \dot{p}_{\text{rms}}^2 = \frac{U_\infty^2 p_{\text{ref}}^2}{D^2} 10^{S_1/10} \quad (21)$$

which yields

$$\frac{\bar{I}_2}{\bar{I}_1} \sim \frac{a_\infty^2 D^2 10^{S_2/10}}{r^2 U_\infty^2 10^{S_1/10}} \sim \frac{1}{M^2 (r/D)^2} 10^{(S_2 - S_1)/10} \quad (22)$$

In this case, with  $M = 0.15$ ,  $r/D \approx 8$  (measured from the end of the cavity to the observer), and  $S_1 \sim S_2$ , the ratio would be  $\bar{I}_2/\bar{I}_1 \approx 0.7$ . This is, at least qualitatively, in agreement with the results in Table 2 and can be taken as an indication that the contributions from terms 1 and 2 are, indeed, affected by cancellations similarly.

The wall-pressure source terms are within about 10 dB of their peak values at  $0 < x_1/D < 29$  and within about 5 dB at  $2 < x_1/D < 12$ .

## B. Viscous Sources

The viscous source strength  $S_4$  is plotted in Fig. 12b. The corresponding plot for  $S_3$  is omitted, partly because of the unimportance of the viscous contribution and partly because  $S_3$  and  $S_4$  look remarkably similar. As expected, the viscous sources are strongest along the wall (as opposed to normal to the wall). The levels are about 25 dB (a factor 1/300) lower than for the pressure sources. Following the preceding arguments, the viscous contribution to the sound intensity at  $x/D = (1, 7.16)$  should then be about 1/300 of the contributions from the pressure sources. Table 2, on the other hand, shows the viscous contribution to be about  $10^{-5}$  of that of the pressure. How can this discrepancy be explained?

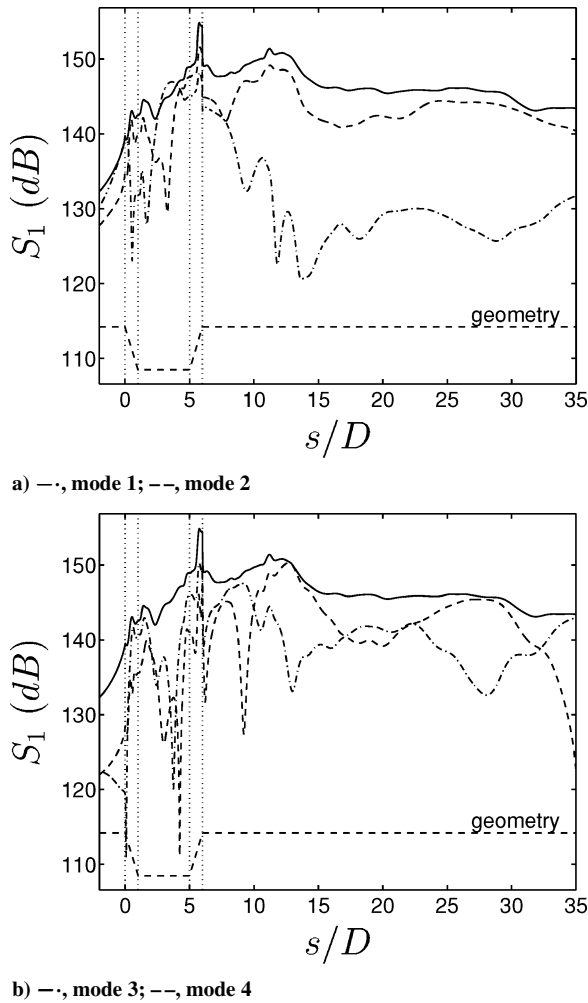


**Fig. 13** Strength of source term 1, modal decomposition: —, total strength.

The critical point here is the fact that the viscous source strength is large along the wall. Because the area radiating to an observer is large when the observer is located nearly normal to the wall but small when the observer is located nearly tangential to the wall, it is clear that the viscous source strength normal to the wall is more relevant in a comparison. The normal source strength is about 55 dB lower than the pressure strength, which corresponds to about  $10^{-5}$  lower intensity.

### C. Correlations

In an attempt to gain further insight into the acoustics of the open cavity, the sound signals at the observers (taken from the DS) are correlated with the dominating sources on the wall, taking the retarded time into account.

The correlation  $R_l(\mathbf{x}, \mathbf{y})$  is defined as

$$R_l(\mathbf{x}, \mathbf{y}) \equiv \frac{\overline{p(\mathbf{x}, t)\Phi_l(\mathbf{y}, t - r/a_\infty)}}{p_{\text{rms}}(\mathbf{x})\Phi_{l,\text{rms}}(\mathbf{y})} \quad (23)$$

where  $p(\mathbf{x}, t)$  is the pressure signal at an observer location from the DS,  $\Phi_l(\mathbf{y}, t - r/a_\infty)$  is a source term at a source location, and the bar denotes a temporal average. The correlations for some observers are plotted in Fig. 14.

Before analyzing the correlations, some thought on what the correlation actually means is necessary. A high value of  $R_l(\mathbf{x}, \mathbf{y})$  means that the signals have similar shapes and phases, which in this case means that the source has acted constructively (or increased the amplitude).  $R_l(\mathbf{x}, \mathbf{y}) < 0$ , on the other hand, means that the source has acted destructively and decreased the amplitude of the radiated signal. Whether the source has made a significant contribution cannot

be determined from the correlation; instead, the source strength in Fig. 12 has to be taken into consideration.

Regardless of observation location, the correlations oscillate around zero downstream of  $x_1/D \approx 10$  (i.e.,  $s/D \approx 12$ ). This is an effect of the vortices being convected along the wall, generating pressure fluctuations as they pass each point on the wall. Because the length scale of these pressure fluctuations is much shorter than the acoustic length scales, the contributions will change from constructive to destructive and back again for different points along the wall.

The source strength is relatively constant downstream of  $x_1/D \approx 12$ , and this fact coupled with the alternating constructive/destructive behavior seen for  $x_1/D > 10$  indicates that this region, despite its large extent and the nonnegligible strength of the source terms, will have little impact on the radiated sound. This was also seen in Fig. 10, where the Curle integral was found to change only moderately past this point.

$R_2$  changes sign at the trailing edge for most observers, which indicates that near-field pressure source  $p$  downstream of the cavity is out of phase with the one inside the cavity.

Another interesting (but rather trivial) observation is the spatial phase difference between  $R_1$  and  $R_2$ ; it is an effect of the temporal phase difference between  $\dot{p}$  and  $p$  (differentiation of a signal with respect to time changes the phase  $\pi/2$ ).

In general,  $R_2$  changes more between different observation locations than  $R_1$  does. An example of this is the region  $x \leq 0$ , where  $R_1$  is positive for observers 1, 4, and 6, but where  $R_2$  changes from positive to negative for the same observers. The reason to this is not known.

### D. Upstream Radiation

The fact that the radiated sound was found to be larger at the upstream observers is easier to understand in the framework of Curle's equation than directly from the DS. In direct simulations, there is no way of telling where the sound originated from, but when using a scalar equation this becomes possible.

The contribution from a wall-pressure source includes a term  $l_i n_i = \cos \varphi$ , where  $\varphi$  is the angle between the wall normal and the direction to the observer. Because of this and the geometry of the cavity, it is clear that the contribution from the downstream cavity wall grows larger upstream. Figure 12a shows that the strongest source,  $S_2$ , has its peak at the downstream cavity wall, which then explains the increased radiation in the upstream direction. The fact that the correlation  $R_2$  at the downstream cavity wall is very high for observer 1, and becomes successively lower for observers 4 and 6, confirms this.

Because  $R_2$  is higher than  $R_1$  for observers 1 and 4, and especially so for the observers farthest upstream, the main contribution to the radiated sound at those observers is that of term 2. Because the contribution from term 2 will disappear at larger distances (because of the  $1/r^2$  factor) and because  $S_1$  has a less pronounced maximum at the downstream cavity wall in Fig. 12a, the upstream dominance is expected to decrease in the far field. This is also seen in Fig. 11a, in which the shape of the OASPL is flatter for the  $\dot{p}$  term.

### E. Volume Sources

The source strength of the volume sources is defined exactly as for the wall sources, that is, by Eq. (19). The reference value is defined in a similar way, so that, for example,  $\Phi_{5,\text{ref}} = p_{\text{ref}}(U_\infty/D)^2$ .

The source strengths of some of the volume sources (the 1,2 components) are plotted in Fig. 15. The volume source terms, especially  $S_5$  (Fig. 15a), have their maximums right behind the cavity. When compared with the instantaneous flowfield in Fig. 6, it is seen that the region of maximum  $S_5$  is located slightly above the path of the vortices ejected from the cavity. This is where the counterclockwise rotating vortices were found to be swept along by the larger vortices, and it is hence hypothesized that this interaction between the vortices is connected to the largest volume sources.

The fact that the source strength is comparatively smaller in the cavity is a somewhat surprising result; after all, that is the region

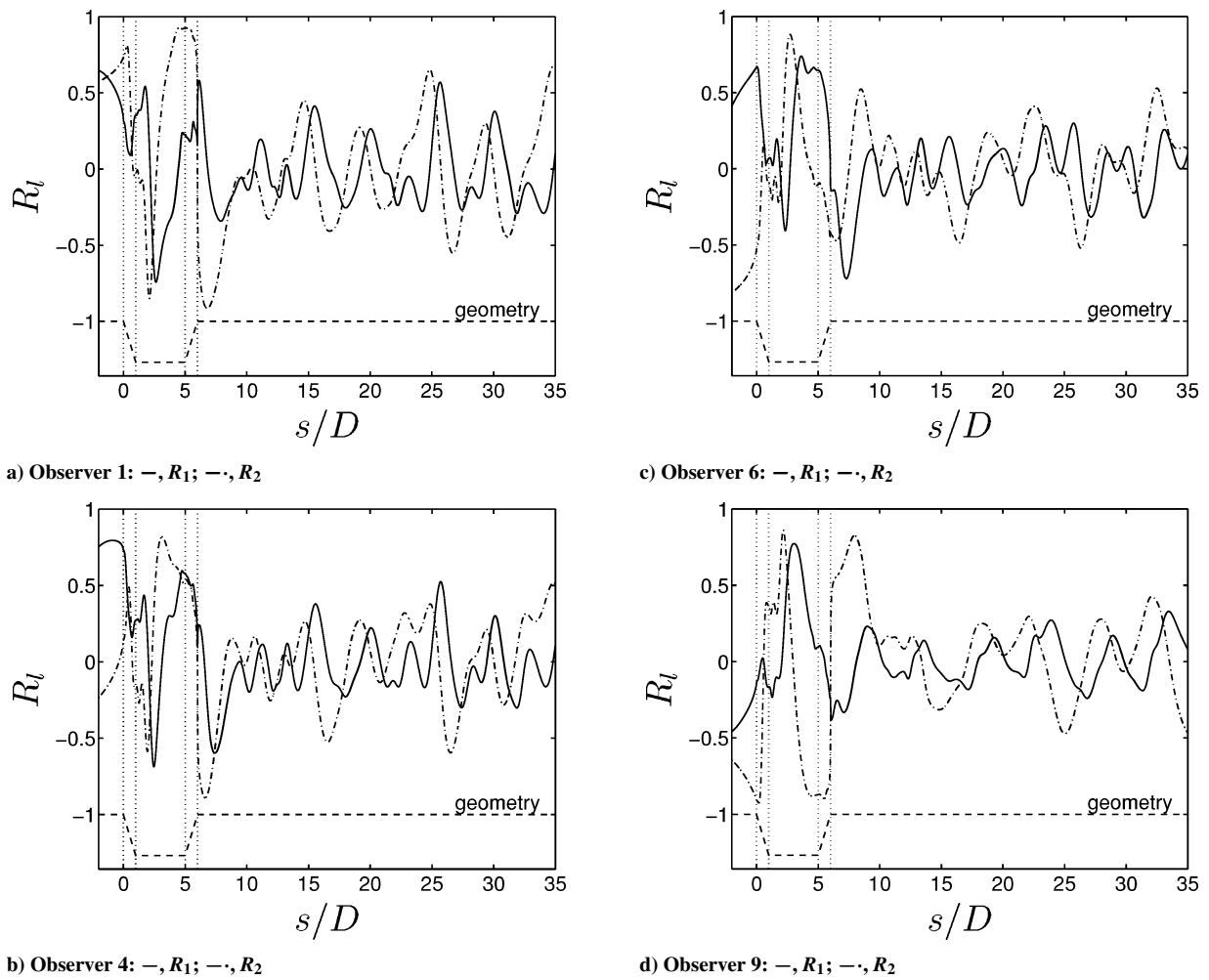


Fig. 14 Correlations between radiated sound and wall source terms.

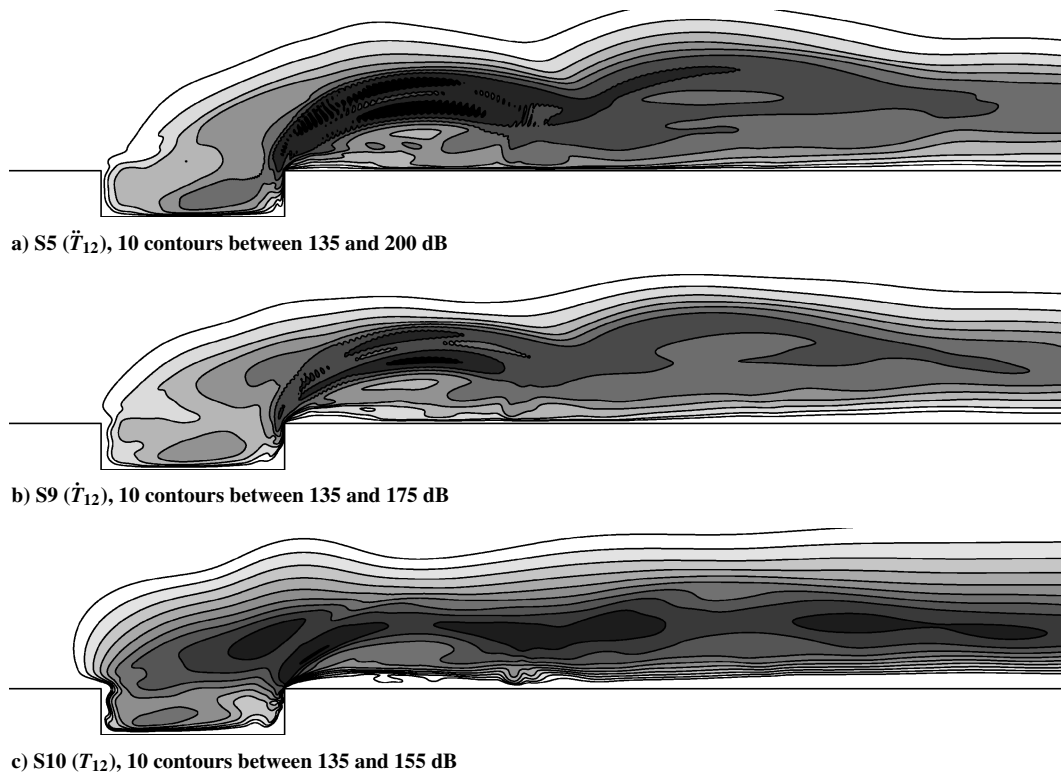


Fig. 15 Volume source strengths.

where the violent ejection of the vortices originates. The explanation could perhaps be that the flowfield in the cavity is built up relatively slowly, whereas it changes more quickly in the region into which the vortices are ejected. This explanation is supported by the fact that the lower-order temporal derivatives of  $T_{ij}$  ( $S_9$  and  $S_{10}$ ) have less pronounced maximums in this region.

Some numerical, high-wave-number, oscillations are present in Fig. 15a but not as much in the other two figures. That the  $\tilde{T}_{ij}$  term is especially affected by these grid-to-grid oscillations is not surprising because the temporal derivatives enhance higher frequencies. Whether these numerical oscillations have an effect on the radiated sound, and if so, how big it is, is not known. They could be removed by adding artificial dissipation, but that would affect the accuracy of the DS adversely.

## VII. Summary

The more general findings of this study can be summarized as follows:

1) The solution of Curle's equation has been written on a form with temporal derivatives, which is valid in the near field, and similar to formulations by for example Brentner and Farassat.<sup>24</sup>

2) The main sources of sound in a low-Mach-number, wall-bounded, flow are the pressure fluctuations on the walls. The viscous contribution on the walls is found negligible because it mainly acts along the walls. The sources in the fluid are small, about 5% of the wall sources for this particular case.

3) The common simplification of Lighthill's tensor  $T_{ij} \approx \rho_\infty u_i u_j$  introduces very small errors at the low Mach number in this case.

4) Being mainly effects of hydrodynamics, the main source terms should be computable from the incompressible equations, but this has not been investigated in this study.

5) The tool of correlations can yield further insight into aeroacoustic noise generation.

6) Curle's equation is, at least in the near field, sensitive to the size of the domain over which the source terms are integrated. This sensitivity, however, is smaller than the sensitivity to boundary conditions of the direct simulation.

The findings on the open cavity are as follows:

1) The sources of sound are largest on the downstream cavity wall. They are also large along the second half of the bottom of the cavity and for about two cavity lengths behind the cavity.

2) The upstream dominance of the radiated sound is explained by noting that the regions of high source strength contribute primarily to the upstream direction.

3) Correlations between the source terms and the radiated sound, coupled with where the sources are large, suggest that the far-field directivity will be flatter.

4) The incoming boundary layer behaves nothing like a flat-plate boundary layer. A consequence of this is that it is hard to specify the boundary-layer characteristics in a nonambiguous way.

5) The sound sources in the fluid, albeit small, are large primarily downstream of the cavity and occur in a region where smaller counterclockwise rotating vortices are being swept along by larger clockwise rotating ones.

## Acknowledgments

This work was supported by Volvo Car Corporation and the Swedish Agency for Innovation Systems.

## References

- <sup>1</sup>Lighthill, M. J., "On Sound Generated Aerodynamically, I. General Theory," *Proceedings of the Royal Society of London*, Vol. A211, No. 1107, 1952, pp. 564–587.
- <sup>2</sup>Phillips, O. M., "On the Generation of Sound by Supersonic Turbulent Shear Layers," *Journal of Fluid Mechanics*, Vol. 9, 1960, pp. 1–27.
- <sup>3</sup>Lilley, G. M., "On the Noise from Jets," AGARD CP-131, March 1974.
- <sup>4</sup>Doak, P. E., "Analysis of Internally Generated Sound in Continuous Materials: 2. A Critical Review of the Conceptual Adequacy and Physical Scope of Existing Theories of Aerodynamic Noise, with Special Reference

to Supersonic Jet Noise," *Journal of Sound and Vibration*, Vol. 25, No. 2, 1972, pp. 263–335.

<sup>5</sup>Curle, N., "The Influence of Solid Boundaries Upon Aerodynamic Sound," *Proceedings of the Royal Society of London*, Vol. A231, 1955, pp. 505–514.

<sup>6</sup>Ffowcs Williams, J. E., and Hawkings, D. L., "Sound Generation by Turbulence and Surfaces in Arbitrary Motion," *Philosophical Transactions of the Royal Society*, Vol. A264, No. 1151, 1969, pp. 321–342.

<sup>7</sup>Larsson, J., "Computational Aero Acoustics for Vehicle Applications," Licentiate Thesis, Dept. of Thermo and Fluid Dynamics, Chalmers Univ. of Technology, Göteborg, Sweden, Nov. 2002.

<sup>8</sup>Gharib, M., and Roshko, A., "The Effect of Flow Oscillations on Cavity Drag," *Journal of Fluid Mechanics*, Vol. 177, 1987, pp. 501–530.

<sup>9</sup>Rockwell, D., and Naudascher, E., "Review—Self-Sustaining Oscillations of Flow past Cavities," *Journal of Fluids Engineering*, Vol. 100, 1978, pp. 152–165.

<sup>10</sup>Ethembaoglu, S., "On the Fluctuating Flow Characteristics in the Vicinity of Gate Slots," Div. of Hydraulic Engineering, Norwegian Inst. of Technology, Technical Rept., Univ. of Trondheim, Trondheim, Norway, June 1973.

<sup>11</sup>Sarohia, V., "Experimental Investigation of Oscillations in Flows over Shallow Cavities," *AIAA Journal*, Vol. 15, No. 7, 1977, pp. 984–991.

<sup>12</sup>Rossiter, J. E., "Wind Tunnel Experiments on the Flow over Rectangular Cavities at Subsonic and Transonic Speeds," Aeronautical Research Council, Repts. and Memoranda, TR 3438, Oct. 1964.

<sup>13</sup>Ahuja, K. K., and Mendoza, J., "Effects of Cavity Dimensions, Boundary Layer, and Temperature on Cavity Noise with Emphasis on Benchmark Data to Validate Computational Aeroacoustic Codes," NASA Rept. CR-4653, 1995.

<sup>14</sup>Rowley, C. W., Colonius, T., and Basu, A. J., "On Self-Sustained Oscillations in Two-Dimensional Compressible Flow over Rectangular Cavities," *Journal of Fluid Mechanics*, Vol. 455, 2002, pp. 315–346.

<sup>15</sup>Shieh, C. M., and Morris, P. J., "Parallel Computational Aeroacoustic Simulation of Turbulent Subsonic Cavity Flow," AIAA Paper 2000-1914, June 2000.

<sup>16</sup>Ashcroft, G., and Zhang, X., "A Computational Investigation of the Noise Radiated by Flow-Induced Cavity Oscillations," AIAA Paper 2001-0512, Jan. 2001.

<sup>17</sup>Eriksson, L.-E., "Development and Validation of Highly Modular Flow Solver Versions in g2dflow and g3dflow," Volvo Aero Corp., Internal Rept. 9970-1162, Trollhattan, Sweden, 1995.

<sup>18</sup>Billson, M., "Computational Techniques for Jet Noise Predictions," Licentiate Thesis, Dept. of Thermo and Fluid Dynamics, Chalmers Univ. of Technology, Göteborg, Sweden, June 2002.

<sup>19</sup>Billson, M., Eriksson, L.-E., and Davidson, L., "Acoustic Source Terms for the Linear Euler Equations on Conservative Form," AIAA Paper 2002-2582, June 2002.

<sup>20</sup>Tam, C. K. W., and Webb, J. C., "Dispersion-Relation-Preserving Finite Difference Schemes for Computational Acoustics," *Journal of Computational Physics*, Vol. 107, No. 2, 1993, pp. 262–281.

<sup>21</sup>Thompson, K. W., "Time Dependent Boundary Conditions for Hyperbolic Systems," *Journal of Computational Physics*, Vol. 68, No. 1, 1987, pp. 1–24.

<sup>22</sup>Colonius, T., Lele, S. K., and Moin, P., "Boundary Conditions for Direct Computation of Aerodynamic Sound Generation," *AIAA Journal*, Vol. 31, No. 9, 1993, pp. 1574–1582.

<sup>23</sup>Gloerfelt, X., Bailly, C., and Juvé, D., "Direct Computation of the Noise Radiated by a Subsonic Cavity Flow and Application of Integral Methods," *Journal of Sound and Vibration*, Vol. 266, No. 1, 2003, pp. 119–146.

<sup>24</sup>Brentner, K. S., and Farassat, F., "Modeling Aerodynamically Generated Sound of Helicopter Rotors," *Progress in Aerospace Sciences*, Vol. 39, No. 2–3, 2003, pp. 83–120.

<sup>25</sup>White, F. M., *Fluid Mechanics*, 3rd ed., McGraw-Hill, New York, 1994, Chap. 7.

<sup>26</sup>Colonius, T., Basu, A. J., and Rowley, C. W., "Computation of Sound Generation and Flow/Acoustic Instabilities in the Flow Past an Open Cavity," American Society of Mechanical Engineers/JSME, FEDSM99-7228, July 1999.

<sup>27</sup>Freund, J. B., "Noise Sources in a Low-Reynolds-Number Turbulent Jet at Mach 0.9," *Journal of Fluid Mechanics*, Vol. 438, 2001, pp. 277–305.

<sup>28</sup>Mankbadi, R. R., Hayer, M. E., and Povinelli, L. A., "Structure of Supersonic Jet Flow and Its Radiated Sound," *AIAA Journal*, Vol. 32, No. 5, 1994, pp. 897–906.

<sup>29</sup>Crighton, D. G., "Basic Principles of Aerodynamic Noise Generation," *Progress in Aerospace Sciences*, Vol. 16, No. 1, 1975, pp. 31–96.

<sup>30</sup>Pierce, A. D., *Acoustics, An Introduction to Its Physical Principles and Applications*, Acoustical Society of America, Woodbury, NY, 1991, Chap. 1.

W. Devenport  
Associate Editor